Chemosphere 264 (2021) 128397

Contents lists available at ScienceDirect

Chemosphere

journal homepage: www.elsevier.com/locate/chemosphere

Graphene oxide transport and retention in biochar media

Md Sazadul Hasan [a], Mengistu Geza [a, *], Jacob B. Petersen [b], Venkataramana Gadhamshetty [a, c]

[a] Department of Civil and Environmental Engineering, South Dakota School of Mines and Technology, 501 East Saint Joseph Street, Rapid City, SD, 57701, United States
[b] Engineering and Mining Experiment Station, South Dakota School of Mines and Technology, 501 East Saint Joseph Street, Rapid City, SD, 57701, United States
[c] 2-Dimensional Materials for Biofilm Engineering Science and Technology (2DBEST) Center, South Dakota School of Mines and Technology, 501 East Saint Joseph Street, Rapid City, SD, 57701, United States

HIGHLIGHTS

- Biochar (BC) offers 250% higher GO retention than sand at 10 mM ionic strength (IS).
- A modified biochar (BC-nZVI) offers 530% higher GO retention at 0.1 −1 mM IS.
- Straining and attachment control GO retention in engineered media.
- Multiple flowrates demonstrate the role of groundwater velocity on GO retention.

GRAPHICAL ABSTRACT

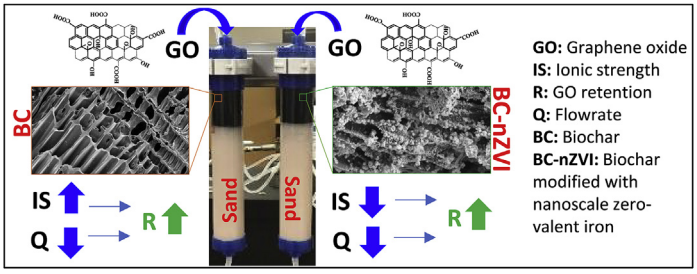

ARTICLE INFO

Article history:
Received 6 July 2020
Received in revised form
11 September 2020
Accepted 20 September 2020
Available online 25 September 2020

Handling Editor: Derek Muir

Keywords:
Nanoparticle transport
Graphene oxide
Biochar
Nanoscale zero-valent iron modified biochar

ABSTRACT

This study explores the use of biochar (BC), an inexpensive filtration media, for removing graphene oxide (GO) contaminants from the aquatic subsurface environments. Mass balance approaches and column dissection tests were used to analyze the retention behavior of GO in a series of model fixed-bed columns as a function of ionic strength (IS) and flowrate. The column based on the biochar media (BC) displayed 3.6-fold higher retention compared to the quartz sand (control). To overcome the challenges of unfavorable electrostatic interactions between GO and BC, we used a facile functionalization strategy to modify the BC surfaces with nanoscale zero-valent iron (BC-nZVI). The BC-nZVI (5:1, w/w) retained 2.6-fold higher amounts of GO compared with bare biochar. Furthermore, the performance of BC-nZVI increased with decreasing values of IS, attributed to the attachment of GO to nZVI where nZVI was partially dissolved by the presence of higher chloride ion at high IS. A better GO retention (86%) at higher IS was observed in BC where the GO was primarily retained due to the higher aggregation via straining.
Published by Elsevier Ltd.

1. Introduction

The global market for graphene materials has been estimated to reach $159 MM by 2023 (Research, 2016). Graphene oxide (GO) precursors are being used to enable inexpensive methods for producing graphene. GO materials display extraordinary properties including small interlayer capillary width (10 Å) and associated impermeability (Smith et al., 2019), high tensile strength (50 GPa for monolayer) (Liu et al., 2012), 100 times higher flexibility

* Corresponding author.
E-mail address: Stu.Geza@sdsmt.edu (M. Geza).

https://doi.org/10.1016/j.chemosphere.2020.128397
0045-6535/Published by Elsevier Ltd.

compared to graphene (Poulin et al., 2016), tunable electrical conductivity (1×10^{-3} to 880 S m^{-1}, an insulator to semi-conductor, respectively) (Huang et al., 2020), high adsorption capacity (~ 1400 mg g^{-1}) (Ali et al., 2019), energy storage capacity (784 mAh g^{-1} after 15 cycles) (Zhu et al., 2010), and excellent fluorescence and photoluminescence (Omidvar et al., 2016). Thus, GO materials are widely used to innovate the components of automobiles, cutting tools, electronics, energy storage, water treatment, imaging, biosensing, and drug-carrier materials (Chen et al., 2020; Wang et al., 2019). The increasing use and production of GO will eventually lead to release into the ecosystem (Avant et al., 2019; Wang et al., 2019), causing potential ecological impacts due to their cytotoxic effects (Akhavan and Ghaderi, 2010) to bacterial (Guo and Zhang, 2017), virus, and mammalian cells (Chen et al., 2020; Liao et al., 2018), plants, invertebrates, and vertebrates (Fadeel et al., 2018). GO materials cause chronic toxicity, lung granuloma, and deaths, as corroborated by the studies based on in vivo tests (Liao et al., 2018; Wang et al., 2011). Thus, it is critical to remove GO materials from impacted waste streams prior to their discharge (Wang et al., 2019; Yuan et al., 2018).

Natural filtration media including sand (Beryani et al., 2020; Lanphere et al., 2013; Wang et al., 2017), limestone (Dong et al., 2017) and clay (Lu et al., 2019) can filter the GO materials. However, the sand filtration media has been reported to fail after passing 2 to 4 pore volumes (PVs) of the solution, where GO was found to be released completely (Beryani et al., 2020; Lanphere et al., 2013) especially when the ionic strength (IS) of the solution was lower than 1 mM. Similarly, the limestone media has also been reported to release ~ 65–100% of GO after > 3 PV for the low IS solutions (< 1 mM) (Dong et al., 2017). Here our goal is to explore the feasibility of using biochar (BC) as a filtration media for retaining GO materials from the aquatic subsurface environment. In addition to the low cost ($350–1200/metric ton) (Thompson et al., 2016), BC offers high specific surface area, cation exchange capacity (Ahmad et al., 2014), and surface roughness (Rodríguez-Vila et al., 2018; Zhang et al., 2018b). Also, BC is amenable to surface modification techniques, for example with nanoscale zero-valent iron (herein referred as BC-nZVI) (Xiong et al., 2019) to remove complex pollutants including heavy metals and nutrients from water and soil (Hasan et al., 2020; Teng et al., 2020; Xu et al., 2020).

We report that a BC-nZVI layer on top of a sand layer can retain GO with a relative concentration (C/C_0) of < 0.05 at lower IS (1 mM), and with 95% of GO retention in the BC-nZVI layer. Conversely, a BC layer demonstrated an exceptional GO retention (C/C_0 ~ 0.15) at higher IS (10 mM). This study sheds light on the transport and retention behavior of GO materials in the BC and BC-nZVI filtration media using simulated parameters that represent realistic aquatic and soil environments (IS = 0.1, 1, and 10 mM and Flow rates = 0.77, 1, and 2 ml min^{-1}) (Chowdhury et al., 2013).

2. Materials and methods

2.1. Materials

A concentrated (5 g L^{-1}) GO suspension with a flake size of 500–5000 nm, a thickness of 1 atomic layer (> 60%), 99% purity that was composed of ≥ 46% C, and ≤ 46% O was used in this study (Item# SKU-HCGO-W-175, Graphene laboratories, NY, USA). The GO suspension of 20 mg L^{-1} was prepared by adding 2 ml of the GO stock solution into nanopure water (> 18.2 MΩ at 25 °C). The mixture was sonicated for an hour at 45 kHz on pulse-mode (10 s on, 5 s off) using an ultrasound probe sonicator (Sonics Vibra-Cell VC 505, USA). The retention and transport behavior of GO was evaluated using pure sand, BC, and BC-nZVI media. Sand and BC were processed (described in section S1) prior to use in the column experiment. The BC-nZVI was synthesized according to the procedure described in section S1 and shown in Fig. 1a.

2.2. Fixed-bed column experiments

The experimental setup and processes based on borosilicate glass columns (DWK Life Sciences, Fisher Scientific, USA) with an inner diameter of 2.5 cm and length of 20 cm, are shown in Fig. 1b and experimental conditions in Table 1. Briefly, the columns were wet packed with the sand, BC, or BC-nZVI media to obtain the following three different configurations: (1) Cleaned and rehydrated sand, (2) a sand column with a layer of BC (5% wt) on the top (BC-sand), and (3) a sand column with a layer of BC-nZVI (5% wt) on the top (BC-nZVI-sand). Potassium chloride (KCl) (research-grade, Fisher Scientific) was used to obtain the electrolytes with different values of IS (10, 1, and 0.1 mM represents high, medium, and low, respectively) based on the IS range in natural aquatic and soil environment (Chowdhury et al., 2013).

The columns were wet packed in DI water with gentle shaking by hand in each cm of media depth to minimize any air entrapment and layering. The stainless steel screens with 50 μm pores were placed at the bottom (outlet) and top (inlet) of the columns to seal and distribute the flow, respectively. We used three flowrates 0.77, 2, and 3 ml min^{-1} in all media types to investigate the effect of flowrate on transport and retention behavior. Recent laboratory studies (Wei et al., 2014; Zhang et al., 2018a) on transport and retention of nanoparticles through subsurface used flowrates ranging from 0.77 to 3 ml min^{-1} representative of flowrates in groundwater (Crittenden and Harza, 2005). A steady flowrate was maintained using a multichannel peristaltic pump (BT100S-1, Golander LLC., Georgia, USA).

The columns were first flushed with >10 pore volumes (PV) of DI water to remove finer impurities, followed by > 4 PV of the desired electrolyte solution to equilibrate the experimental conditions. Then, GO solution of 10–30 PV (Table S1) along with the desired electrolyte was introduced into the respective columns as defined in Table 1. The influent GO solution was simultaneously sonicated using a water bath (40 kHz, Branson 2510) to prevent any prior aggregation issues. To study the retention of GO in the media, the 4 PVs of the electrolyte was introduced after each run. Effluent samples from the columns were collected every 5–15 min and analyzed to measure the GO concentrations. The breakthrough curves (BTCs) for GO transported through column media were plotted as the relative concentrations (ratio of the effluent and initial GO concentrations, C/C_0) as a function of PVs of solution passing through columns.

To quantify the spatial distribution of retained GO mass, the column materials were dissected immediately after the transport experiment (details in section S2). The mass of retained GO in each at 4 cm of the sand layer was used to plot GO retention profiles (RPs) along the sand profile. RPs denoted the mass of GO retained per unit mass of sand as a function of column length. Considering that BC and BC-nZVI layers (~4 cm) on the sand were deliberately removed for characterization, the mass of GO retained in BC and BC-nZVI layers are not shown in RPs. Hence, the retained GO mass in the BC and BC-nZVI was determined by tracking and balancing the total GO mass in the influent, remaining sand layers, and effluents and compared to the homogeneous sand column data with the same experimental conditions as control (Table 1).

2.3. Analytical methods and characterization

Fourier transform infrared spectroscopy (FTIR), Raman spectrophotometer, X-ray fluorescence (XRF), Field emission scanning electron microscopy (FE-SEM) equipped with an energy dispersive

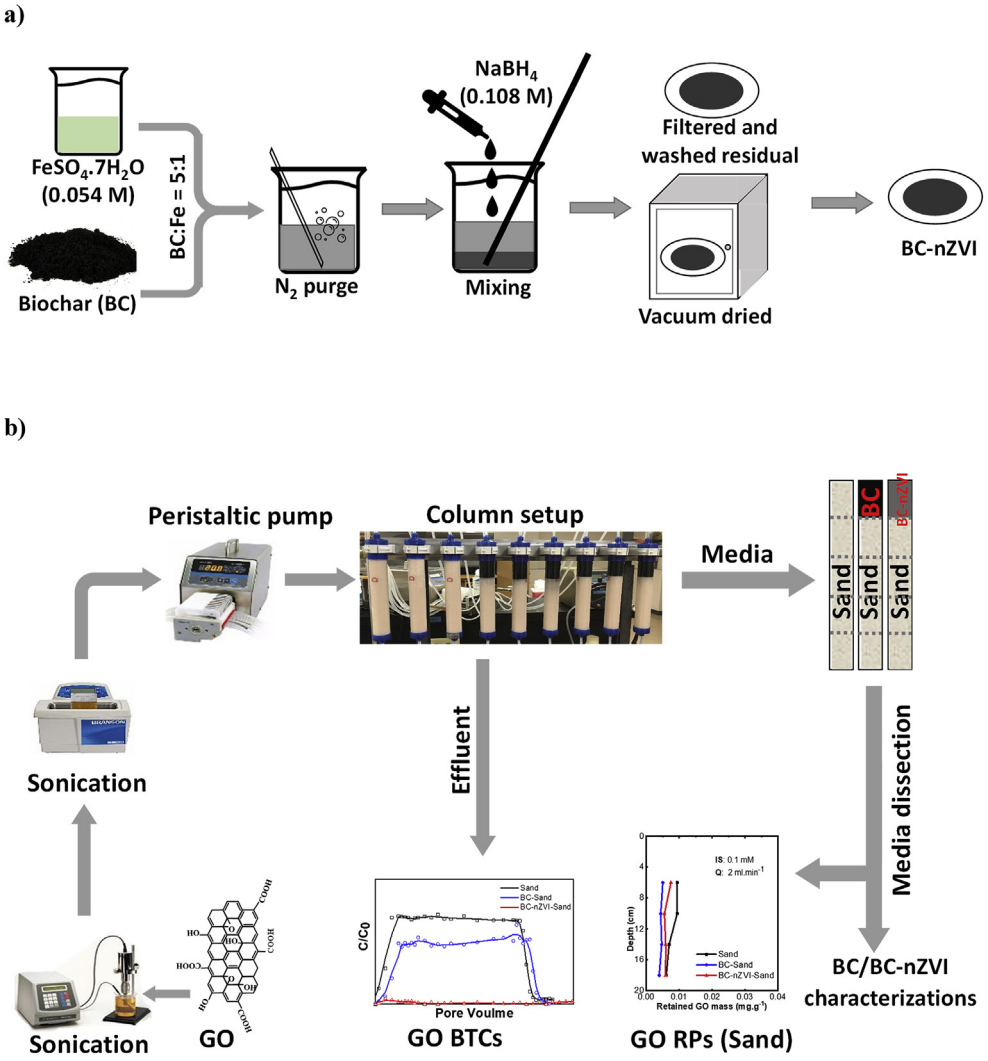

Fig. 1. a) Synthesis process of BC-nZVI and b) A schematic diagram of the column experiments.

X-ray spectrometer (EDS), and Brunauer–Emmett–Teller (BET) techniques were used to identify the characteristics of BC and BC-nZVI. The GO concentration was measured using an ultraviolet–visible (UV) spectrophotometer (Fig. S1) and the electrokinetic properties of GO and zeta potentials of media using a Zetasizer. Detailed information on these techniques is presented in section S3.

3. Results and discussion

3.1. Electrokinetic and hydrodynamic properties of GO

To study the aggregation behavior of GO, we assessed the electrokinetic and hydrodynamic properties of GO under the IS range of 0.1–10 mM, a range typical to natural water systems (Chowdhury et al., 2013). The increase in IS beyond 0.1 mM resulted in an electrical double layer compression, larger distribution in EPM, and an increase in hydrodynamic diameter (Lanphere et al., 2013). Due to the reduced GO-GO electrostatic repulsive forces at higher IS (Lanphere et al., 2013; Liang et al., 2019), the hydrodynamic diameter at 1 mM (600 nm) was 2.5-fold higher than that at 0.1 mM (250 nm) in 60 min which was further increased with time (Fig. S2a). It is expected that GO aggregates at a higher IS due to the reduced energy barrier and greater depth of the secondary minimum. We used this information to interpret the micropore structure and surface roughness needed by BC to strain and retain GO. The EPM (Fig. S2b) of GO was less negative at high IS (10 mM) compared to low (IS 0.1 mM), $(-3.54 \pm 0.05) \times 10^{-8}$, and $(-3.02 \pm 0.12) \times 10^{-8}$ m^2 V^{-1} s^{-1} respectively. Thus, GO is likely stable in natural aquatic environments which are typically dominated by the monovalent K^+ cation.

To evaluate the effect of GO and media surface potentials on surface interactions, the ζ-potentials of the GO, sand, BC, and BC-nZVI were assessed and compared under different experimental conditions (Table S2). In general, the negative value of ζ-potentials implies a repulsive particle to particle and particle to media electrostatic interaction, resulting in unfavorable conditions for attachment. At 0.1–10 mM IS, both the GO and the filtration media (sand, BC, and BC-nZVI) displayed negative charges, suggesting unfavorable conditions for GO attachment at higher IS. However, an increase in IS also resulted in decreased negative charges on GO, an observation consistent with the previous study (Chowdhury et al., 2013).

Here a key finding is that the ζ-potential for BC and BC-nZVI was

Table 1
Summary of the column experiments.

[a]Exp.	KCl (mM)	Flowrate (ml min^{-1})	[b]EBCT (min)	pH	Media configuration	[c]$R_{0-4\ cm}$ (%)	[d]$R_{4-20\ cm}$ (%)	[e]R_E (%)	[f]R_T (%)
1	0.1	2	49.09	5.9	Sand	4.29	11.68	98.35	114.32
2					BC on Sand	31.96	6.94	75.42	114.32
3					BC-nZVI on Sand	96.06	4.65	13.61	114.32
4	1	2	49.09	5.7	Sand	6.54	20.07	80.55	107.16
5					BC on Sand	40.27	13.43	53.46	107.16
6					BC-nZVI on Sand	82.47	7.95	16.73	107.16
7	10	2	49.09	5.6	Sand	7.43	20.38	83.76	111.58
8					BC on Sand	86.47	13.62	11.48	111.58
9					BC-nZVI on Sand	85.42	4.14	22.02	111.58
10	1	0.77	127.50	5.7	Sand	7.21	22.37	77.98	107.56
11					BC on Sand	59.47	26.00	22.08	107.56
12					BC-nZVI on Sand	96.42	6.59	4.54	107.56
13	1	2	49.09	5.7	Sand	6.54	20.07	80.55	107.16
14					BC on Sand	40.27	13.43	53.46	107.16
15					BC-nZVI on Sand	82.47	7.95	16.73	107.16
16	1	3	32.72	5.7	Sand	4.59	13.71	92.24	110.54
17					BC on Sand	41.55	7.63	61.36	110.54
18					BC-nZVI on Sand	81.86	3.54	25.14	110.54

[a] Each column experiment was duplicated and the influent concentration was 20 mg L^{-1}.
[b] EBCT: Empty Bed Contact Time (min).
[c] $R_{0-4\ cm}$: GO recovered from the top 4 cm sand, BC, and BC-nZVI layers (based on column configuration).
[d] $R_{4-20\ cm}$: GO recovered from sand columns from 4 to 20 cm starting from the top of the column.
[e] R_E: GO recovered from the effluent, calculated from the effluent GO concentration and volume.
[f] R_T: Percent of total GO mass recovered.

less negative compared to the sand media at both low and high IS conditions. At higher IS (10 mM), the ζ-potentials for BC and BC-nZVI were −22.17 and 0.22 mV respectively compared to −30.80 mV for sand. The more positive the ζ-potentials values the more favorable is the adsorption of negatively charged GO onto the filtration media.

3.2. Biochar media characteristics

It is evident from FTIR results (Fig. 2a) that, both BC and BC-nZVI surfaces have O–H (~3425 cm^{-1}), –COOH (~1362, 1378, 1614, and 1627 cm^{-1}), and C–C, C–O, or C–O–C (~1089 cm^{-1}) bond vibrations, however, the BC-nZVI contained additional peaks at 617 and 705 cm^{-1} indicating the formation of Fe–O (Prabu et al., 2017). The

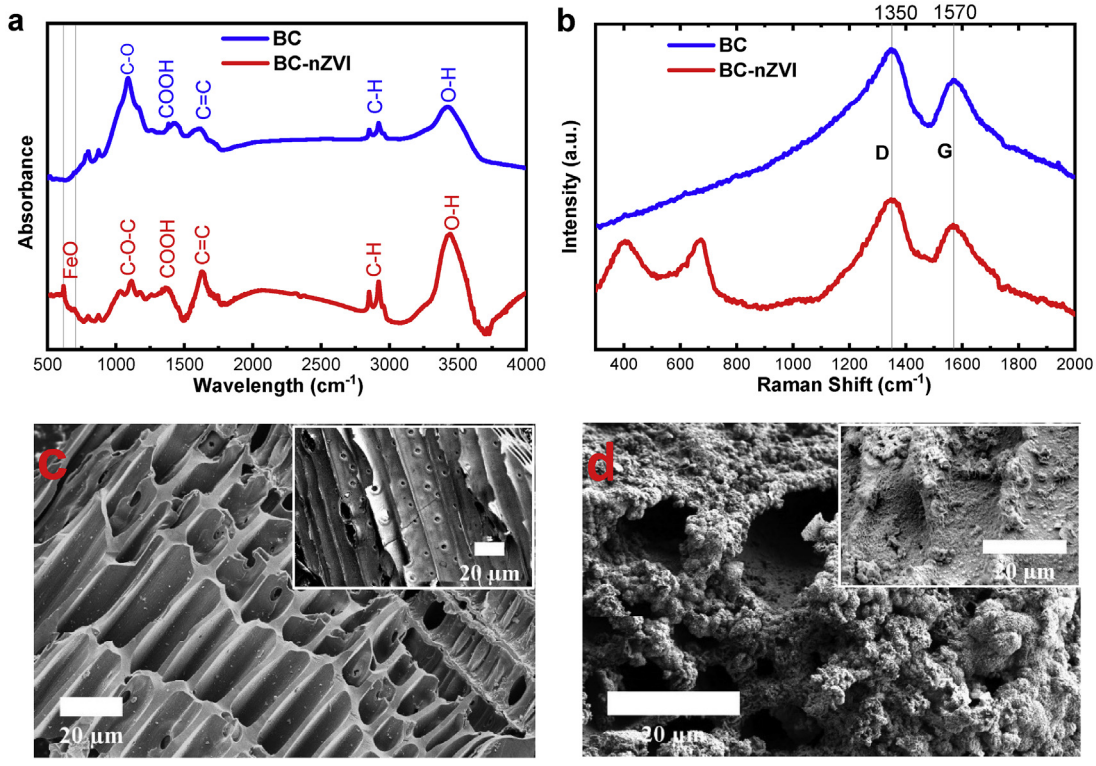

Fig. 2. a) FT-IR spectra of BC and BC-nZVI, b) Raman spectroscopy of BC and BC-nZVI, c) BC SEM images, and d) synthesized BC-nZVI SEM images.

presence of iron on the BC-nZVI surfaces was corroborated by the Raman spectra analysis (Fig. 2b). The 1350 (D band) and 1570 (G band) cm^{-1} peaks correspond to the defects and graphite-like structures, respectively. The I_D/I_G ratio for BC-nZVI (1.22) was substantially lower than BC (1.31), corroborating the attachment of nZVI on the biochar surfaces (Norouzi and Di Maria, 2018). The additional peaks at 425 and 685 cm^{-1} were attributed to the presence of iron composites that were added to the biochar surfaces (Norouzi and Di Maria, 2018).

Upon the modification with nZVI, the biochar surface underwent significant morphological changes. Biochar displayed a macroporous and rough surface with distinct channels (Fig. 2c; see the inset for macropores); whereas BC-nZVI evolved into a rough surface with well-distribution iron particles (Fig. 2d). BC-nZVI revealed higher levels of iron (18 & 30%) compared to biochar (1.44 & 0.5%), based on the XRF analysis and EDS mapping analysis, respectively (Table S3). The SEM-EDS results confirmed homogeneous iron coating on the surface of BC-nZVI (Fig. 3). The BC-nZVI was characterized by reduced surface area and pore volume (Table S4 and Fig. S3, BET analysis) due to the plugging of macro and micropores in BC with nZVI particles. The specific surface area of BC-nZVI decreased from 76.21 to 23.94 $m^2\ g^{-1}$ and the total pore volume from 0.05 to 0.02 $cm^3\ g^{-1}$, creating a favorable condition for straining.

3.3. Effect of solution chemistry

We assessed BTCs and RPs of GO, based on the relative concentrations and mass retention from the three different column studies and at different values of IS (Fig. 4). The transport and retention behavior of GO in BC-sand and BC-nZVI-sand was influenced significantly under typical environmental aquatic ionic strengths, compared to bare sand. For example, changing the IS from 10 mM to 0.1 mM changed the peak breakthrough levels for sand only by 6% (from 93 to 100%), after the passing of at least 2 PV of GO solution. Transport studies in sand columns with similar sand particle sizes also showed poor GO interactions at IS less than 10 mM (French et al., 2009; Lanphere et al., 2013).

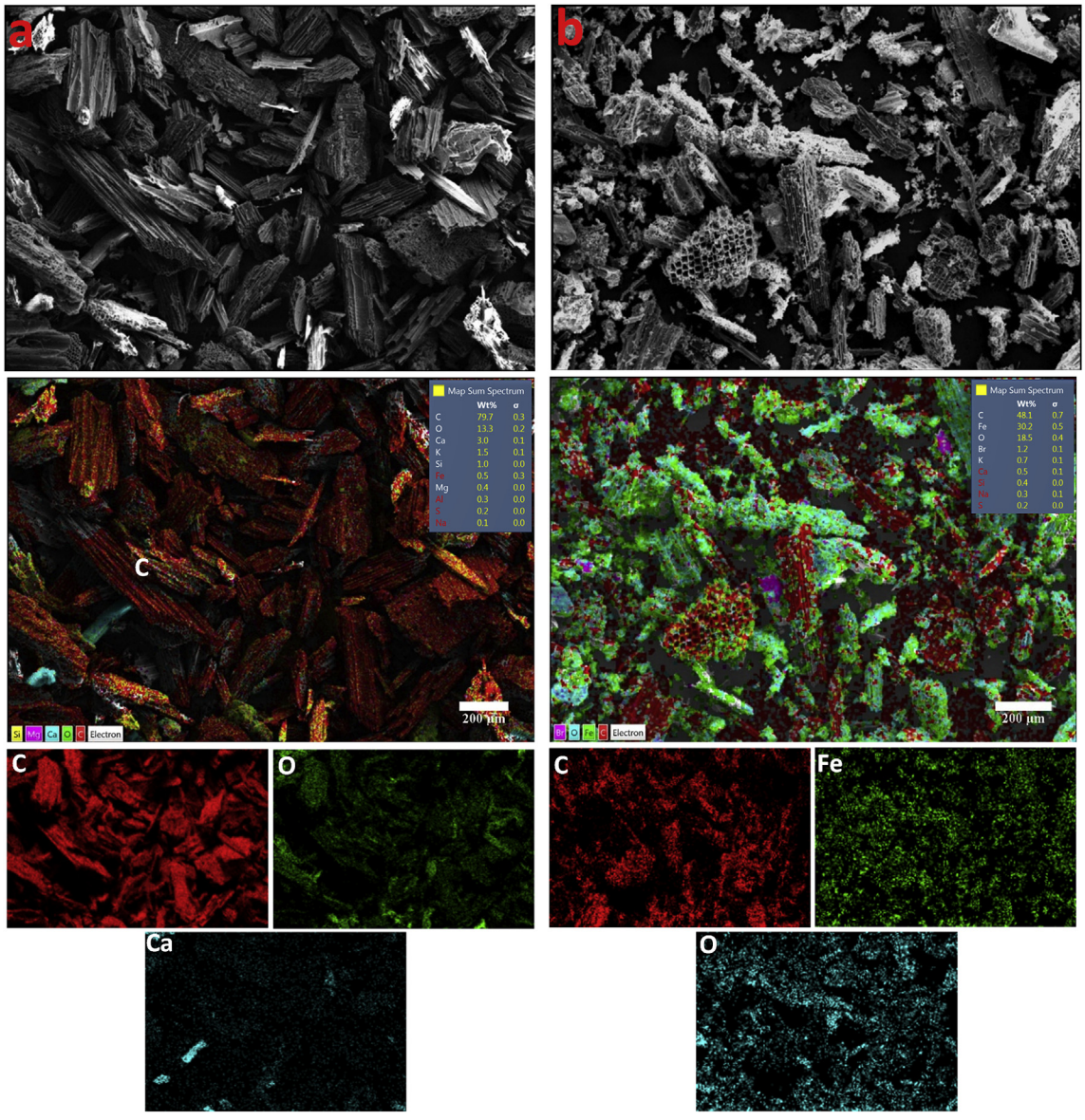

Fig. 3. SEM-EDS mapping of a) BC and b) synthesized BC-nZVI.

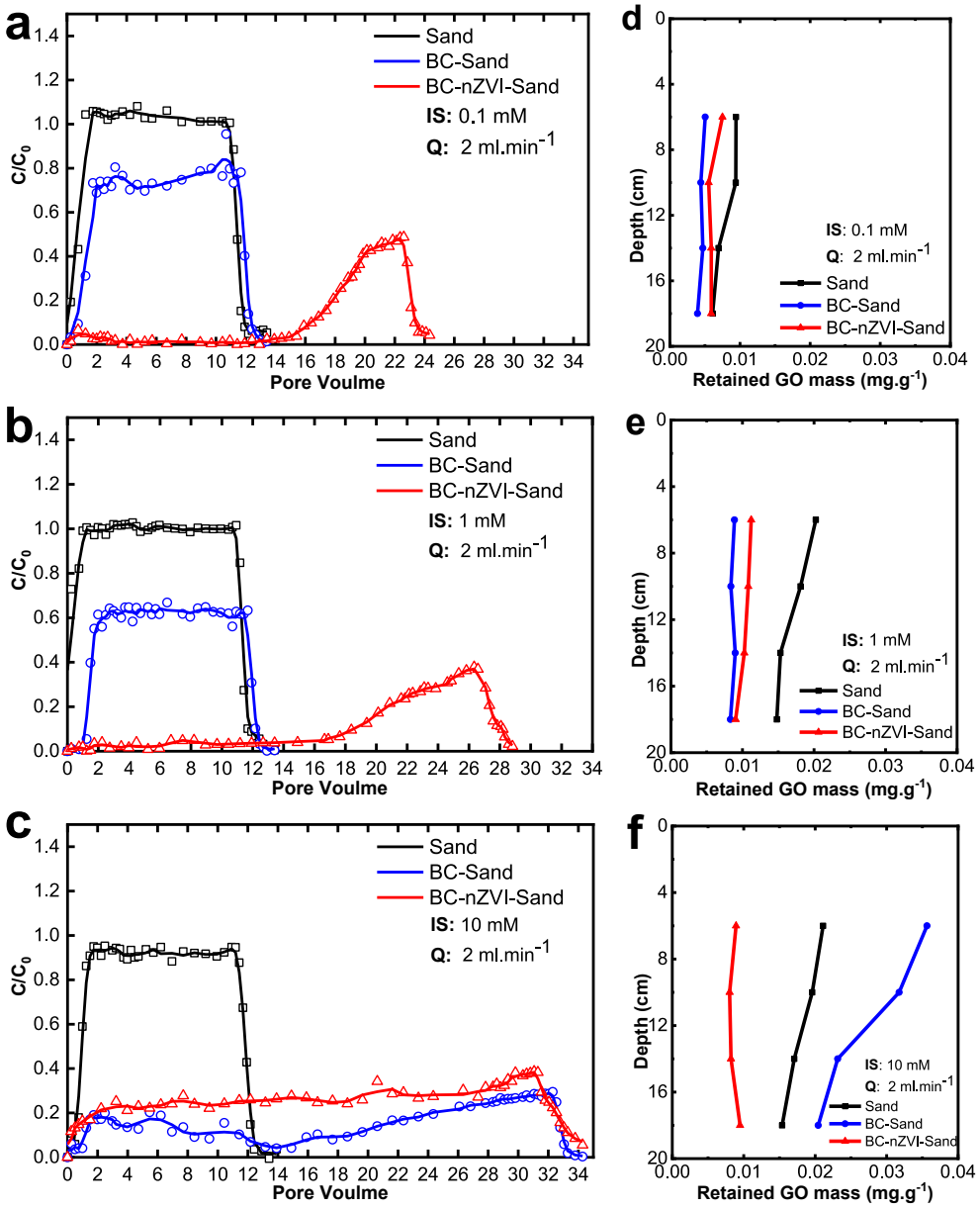

Fig. 4. (a, b, and c) Breakthrough curves and (d, e, and f) retention profiles of columns with different solution IS at the background with constant flowrate (Q = 2 ml min^{-1}) and influent GO concentration (20 mg L^{-1}).

BTC showed the lowest (C/C_0 = 0.15 on average) relative concentration in the BC-sand column at 10 mM IS, suggesting an increased GO retention in the BC-sand column compared to the sand column at higher solution IS. Note that the initial breakthrough in BC-sand columns occurred at the same time as sand columns, but with low maximum relative concentrations (C/C_0) (0.73 vs 1.05 and 0.60 vs 0.99 at 0.1 and 1 mM respectively).

The GO transport and retention behavior in the BC-nZVI-sand column were counter-intuitive compared to the BC-sand column. Higher GO retention in BC-nZVI at $\leq$ 1 mM, indicating the BC-nZVI as an efficient media for retaining GO at lower IS. As shown in Fig. 4, negligible levels ($C/C_0 < 0.05$) of GO were observed in the effluents from BC-nZVI-sand columns after the passing of at least 16 PV of GO solution at $\leq$ 1 mM. The relative concentrations reached a maximum of 0.43 and 0.35 at IS 0.1 and 1 mM respectively after 22 and 27 PV of GO solution passed through the column. Surprisingly, at IS of 10 mM, GO broke through relatively early in BC-nZVI-sand column after passing only 2 PV of GO solution with a relative concentration (0.18–0.25) after running of 32 PV of GO solution. The variation of GO transport behavior in BC-nZVI-sand column occurred because of the surface interaction of GO and BC-nZVI (explained in Section 3.5). GO and BC-nZVI interaction at 10 mM likewise affects the initial GO breakthrough time for BC-nZVI-sand columns (described in section S4 and Fig. S4a).

The mass balance of GO from column dissection data illustrated the amount of GO mass eluted and retained in each of the media and presented in Table 1. The mass balance ranged from 107 to 114% of the total GO mass injected to the column which agrees with the recovery trend previously reported (Lanphere et al., 2013; Sun et al., 2015). However, GO displayed a tendency to be weakly retained on the sand in limited amounts and poorly interacted at all ISs which is consistent with previous studies (Chen et al., 2018; Lanphere et al.,

2013). Therefore, the total GO mass retention was less in the sand column compared to other columns. IS exhibited an enormous effect on the GO mass retention in BC/BC-nZVI media which agrees with the finding from BTCs. GO mass retained in Sand, BC, and BC-nZVI layers (the top 4 cm) were compared. GO mass retained in BC and BC-nZVI layers was considerably higher compared to the sand layer for all IS ranges but the retention behavior varied with IS. For example, GO mass retention at 10 mM was about 86.5%, 85%, and 7.5% of the injected GO in BC, BC-nZVI, and sand layers respectively, whereas, at 0.1 mM, the BC layer retained only about 32% compared to 96% in BC-nZVI layer and the sand layer retained 4%. The higher retention in BC layer at higher IS is attributable to higher aggregation at higher IS. Higher retention (96%) was observed in BC-nZVI layer at lower IS attributable to favorable chemical interactions between GO and nZVI. Although a weaker GO aggregation was observed at 0.1 mM, the porosity and surface roughness of BC resulted in significant retention (32%) than sand with retention of only 4%.

RPs in the bottom 16 cm sand layer is shown in Fig. 4 d, e, and f for Sand, BC-sand and, BC-nZVI-sand columns, indicating the mass retention decreased with depth in all columns. In the sand column, the maximum GO retention in 4–8 cm sand layer twice as high (0.011 versus 0.024 mg g^{-1}) for IS of 10 mM compared to 0.1 mM, attributable to the aggregation of GO with increasing IS and retained to immediate layer. We observed that GO mass retained in the bottom 16 cm sand layer was high for the sand columns compared to BC-sand and BC-nZVI-sand columns. This was likely due to higher retention in the top BC and BC-nZVI layers which lowered the amount of GO released to the subsequent sand layers in BC-sand and BC-nZVI-sand columns. However, the highest retention was observed in the BC-sand column at 10 mM. This could be attributed to both BC pore size and GO aggregation behavior (described in section S5).

Remarkably, GO retention in the sand layers below BC-nZVI layer did not show any significant (0.006–0.009 mg g^{-1}) shift with the change in IS and BTCs proved that there was negligible GO detected in the effluent (high retention) of BC-nZVI-sand column at 0.1 and 1 mM. Therefore, it can be concluded that a greater portion of GO was retained in BC-nZVI layer at 0.1 and 1 mM IS. Additionally, compared to lower IS (0.1 and 1 mM) more GO was released from the BC-nZVI layer at higher IS (10 mM) which was not retained considerably in subsequent sand layers due to the altered GO surface and solution properties (described in subsequent section 3.5).

3.4. Effect of flowrates

Lower flowrate increases the empty bed contact time (EBCT), resulting in an increase in GO-media interaction and GO retention. The BTCs and RPs for different flowrates into the columns shown in Fig. 5 suggested that the transport and retention behavior of GO in BC-Sand and BC-nZVI-sand columns were influenced by the column inflow rate at 1.0 mM IS primarily due to variable interaction time and site blocking. BTCs for sand columns revealed, lower flowrate (0.77 ml min^{-1}) resulted in more particle interaction time (EBCT ~ 127.5 min) but the maximum relative concentration did not change significantly (C/C_0 ~ 1.0 in all cases) compared to flowrate 2 and 3 ml min^{-1}. This demonstrated the limited interaction of GO with sand which was reported by recent studies (Qi et al., 2019). Likewise, RPs showed poor retention which was consistent (~0.02 mg g^{-1}) at 0.77 and 2 ml min^{-1} flowrate and further decreased to 0.012 mg g^{-1} at 3 ml min^{-1} due to high pore velocity.

However, GO exhibited an exceptional surface interaction (described in section 3.5) with BC/BC-nZVI media which varied at different flowrates and affected retention behavior. For example, BC-sand column displayed higher retention (C/C_0 = 0.4 vs 0.6) in BTCs at a flowrate of 0.77 and 2 ml min^{-1} respectively which was further increased to 0.77 at 3 ml min^{-1}. The EBCT increased by 3.9-fold (32.72–127.50 min) (Table 1) when the flowrate was reduced from 3 to 0.77 ml min^{-1}. The increase in EBCT enhanced the intraparticle interaction and physical adsorption in highly porous and rough-edged BC. The reduction in flowrate from 3 to 0.77 ml min^{-1} increased the breakthrough time from 45 to 130 min as shown in Fig. S4b. Also, the increased interaction time at 0.77 ml min^{-1} increased the retention of GO in the sand layer under BC shown in RPs which was reduced (0.02–0.007 mg g^{-1}) with the flowrate increased to 3 ml min^{-1}. It was noticed in the BC-nZVI-sand column that, there was almost no breakthrough (C/C_0 = 0.05) after running 30 PV at a lower flowrate (0.77 ml min^{-1}). Nevertheless, GO breakthrough occurred after 18 and 5 PV of GO when the flowrate increased to 2 and 3 ml min^{-1}, respectively. Also, at a flowrate of 3 ml min^{-1}, the relative concentration reached 0.10 from 5 to 25 PV of GO. However, GO transport and retention were substantially affected by the flowrate after 18 and 25 PV of GO was run at 2 and 3 ml min^{-1} respectively. Minimal GO release at low flowrates was attributed to the partial influence of the solution chemistry to GO, nZVI, and sand surface at 1 mM IS which was much more at 10 mM. Therefore, higher flowrate decreased the particle interaction time and increased site-blocking (Messina et al., 2015), which was predominantly led to the reduction of GO retention in contrast to the lower flowrate. Column dissection revealed the mass (Table 1) of GO retained in BC and BC-nZVI layer decreased ~31% and 15% respectively when the flowrate increased from 0.77 to 3 ml min^{-1} which also supports the findings from BTCs and RPs at different flowrates.

3.5. Interaction mechanisms

The exponentially increase in the retention of GO in BC media is primarily due to the GO-GO and GO-media interactions (Fig. S5), which are significantly influenced by the solution chemistry. When GO suspension was initially introduced into the solution, the K^+ ions occupied the functional groups (carboxyl, hydroxyl, etc.) that were present on the GO surface. The GO and BC surface turned less negative at higher IS, increasing the GO-GO and GO-BC interactions in the solution. The high surface roughness of BC increased the physical adsorption of GO and high porosity (macro and micro-pores) helped BC retain more GO due to straining via aggregation at higher IS. The retention of GO on BC at high IS contributed to the aggregation behavior of GO along with the physical adsorption on the surface. At lower IS, some portion of GO will still attach to the BC surface, but most of it will pass through the pores as the particle sizes are smaller compared to sizes at high IS.

Transport of GO in BC-nZVI was dramatically changed due to the chemical interactions of GO, nZVI, and chloride ions in the solution at different IS. When the GO solution passed through BC-nZVI-sand there was physical adsorption due to the porosity and surface adsorption at any IS level. However, the retention of GO in BC-nZVI was further dominated by the interaction of GO and nZVI at different IS levels. For example, high GO retention in BC-nZVI at lower IS was attributed to the attachment of GO to Fe^0 and retained on the surface. As evident, the presence of C on the nZVI surface confirms the attachment of GO sheets onto BC-nZVI (Fig. S6) at lower IS. At higher IS, the chemical interaction between chloride ions and nZVI became prominent which affected the subsequent IS and pH of the solution. Hence, abundant chloride ions interacted with the nZVI and detached from the BC surface due to increased electron transfer (Kim et al., 2016), followed by dissolution to the influent solution and flow through the column media. It has also been reported that the presence of Cl^- ions at high concentration

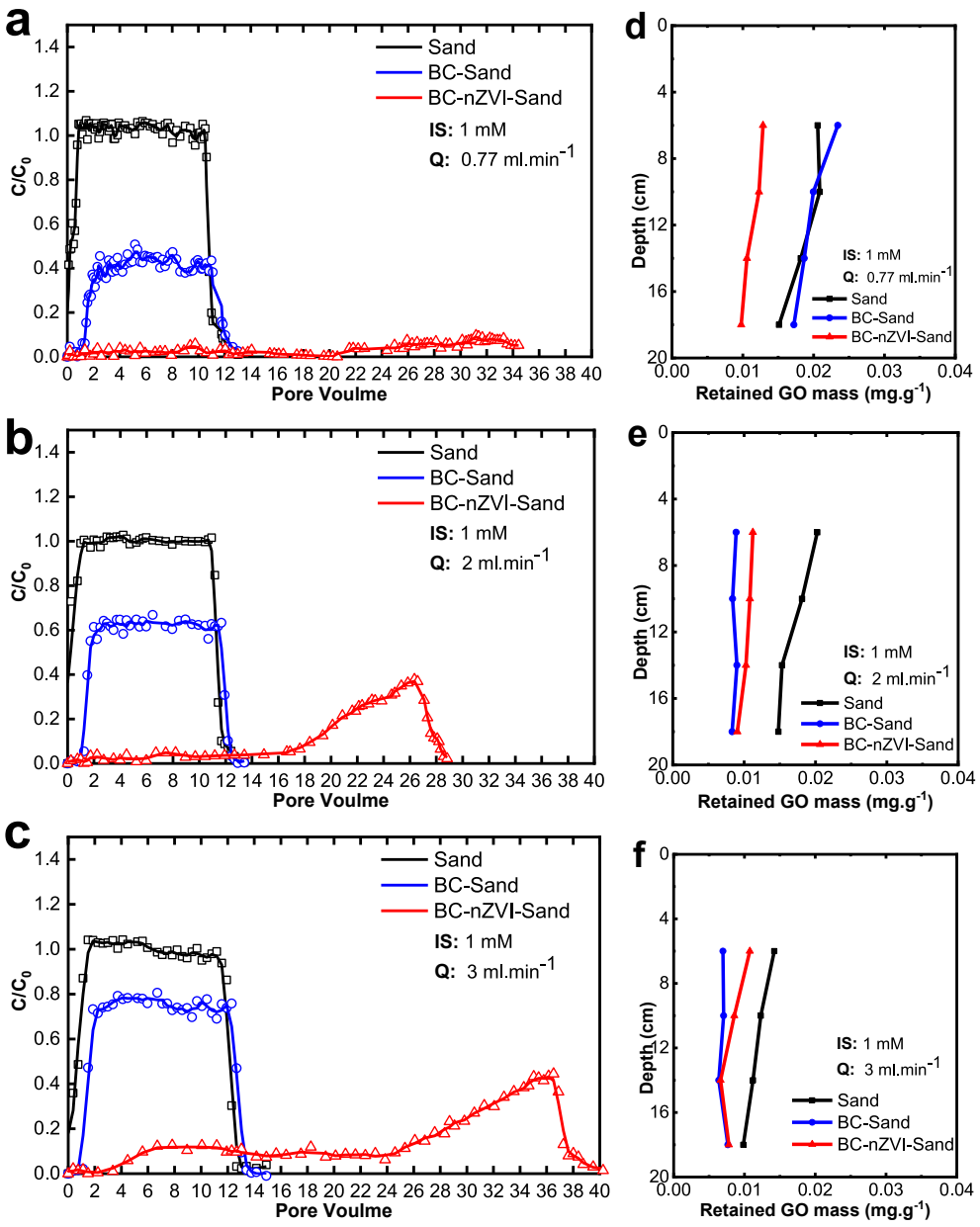

Fig. 5. (a, b, and c) Breakthrough curves and (d, e, and f) retention profiles of columns with different inflow rates (Q) with constant IS (1.0 mM) and influent GO concentration (20 mg L^{-1}).

encouraged Fe^0 corrosion at higher IS (Ma, 2012; Sleiman et al., 2017). SEM-EDS mapping (Fig. S7) of the BC-nZVI surface after the transport experiments at lower and higher IS revealed that the presence of nZVI on BC-nZVI surface decreased at higher IS. Therefore, GO was retained in BC-nZVI at the beginning but started releasing with increasing IS. However, the GO retention ($C/C_0 < 0.4$) in Sand-BC-nZVI column at 10 mM is attributed to the electrostatic attraction between GO and remaining nZVI on BC-nZVI where the solution would become more acidic due to the chloride ions interaction with nZVI. The similarity in functional groups on deposited GO and the BC made it difficult to capture changes in the FTIR spectra (Fig. S8a) for the exposed BC. In contrast, FTIR spectra of the exposed BC-nZVI (Fig. S8b) displayed a shift in peaks in the range of 550–750 cm^{-1} at higher and lower IS values, confirming the attachment of GO to Fe. However, the lower intensities in peaks at higher IS compared to lower IS confirms the presence of Fe was decreased at higher IS. Additionally, the presence of Fe–Cl compounds in the effluent at higher IS observed by UV spectroscopy agrees with that finding. The peaks at 310 nm and 468 nm (Fig. S9) confirms the presence of Fe–Cl compounds (Abbott et al., 2017; Calandra et al., 2015) in the effluent whereas no Fe–Cl was found in the effluent at lower IS.

Finally, psychochemical interactions of GO with BC and BC-nZVI suggested an inverse GO retention behavior as a function of IS. This key retention behavior suggests that a media with BC and BC-nZVI configured in a series can efficiently retain GO under a range of natural and engineered solution IS.

4. Conclusion

This study demonstrates the unique retention behavior of GO in the modified biochar media compared to typical sand filtration

media. The functionalized form of biochar (BC-nZVI) displayed higher surface roughness and enhanced chemical interactions, promoting the GO transport and retention in BC-nZVI. We report a distinct chemical behavior of nZVI at a different level of the ionic strength. At lower IS (0.1–1 mM), BC-nZVI displayed improved surface roughness and favorable surface interactions of nZVI with GO. However, at high IS (10 mM) the GO interactions with nZVI onto BC-nZVI were constrained, likely due to the corrosion and subsequent dissolution of Fe^0 exposed to the high levels of chloride ions. The lower mobility (higher retention) of GO in BC-nZVI at the lower IS, and similar phenomena for BC at the higher IS, revealed the unique transport and retention behavior of GO in biochar media. Lower flowrates increase GO aggregation due to increased EBCT time, which subsequently decreased transport and increased GO retention. Conversely, increased flowrate, having site-blocking effect, reduced GO retention in biochar media. These findings can be used to improve the design configuration for the treatment of GO-laden waste streams. Additionally, the use of inexpensive biochar and the nZVI modifiers can render the altered media an effective material to prevent water resource contamination by emerging nanoscale GO use.

Credit author statement

Md Sazadul Hasan: Conceptualization, Methodology, Laboratory experiments, Data analysis, Material characterizations, Data presentations, Writing original draft, Writing - Review & Editing. Mengistu Geza: Conceptualization, Methodology, Funding acquisition, Data presentations, Supervision, Resources, Project administration, Writing - Review & Editing. Jacob B. Petersen: Material characterizations, Writing - Review & Editing. Venkataramana Gadhamshetty: Conceptualization, Resources, Writing - Review & Editing.

Declaration of competing interest

The authors declare that they have no known competing financial interests or personal relationships that could have appeared to influence the work reported in this paper.

Acknowledgments

This research was supported by the Water Resources Foundation, Nelson Research Grant, and the National Science Foundation under research grants NSF RII T-1 and T-2.

Appendix A. Supplementary data

Supplementary data to this article can be found online at https://doi.org/10.1016/j.chemosphere.2020.128397.

References

Abbott, A.P., Al-Bassam, A.Z., Goddard, A., Harris, R.C., Jenkin, G.R., Nisbet, F.J., Wieland, M., 2017. Dissolution of pyrite and other Fe–S–As minerals using deep eutectic solvents. Green Chem. 19 (9), 2225–2233.
Ahmad, M., Rajapaksha, A.U., Lim, J.E., Zhang, M., Bolan, N., Mohan, D., Vithanage, M., Lee, S.S., Ok, Y.S., 2014. Biochar as a sorbent for contaminant management in soil and water: a review. Chemosphere 99, 19–33.
Akhavan, O., Ghaderi, E., 2010. Toxicity of graphene and graphene oxide nanowalls against bacteria. ACS Nano 4 (10), 5731–5736.
Ali, I., Mbianda, X., Burakov, A., Galunin, E., Burakova, I., Mkrtchyan, E., Tkachev, A., Grachev, V., 2019. Graphene based adsorbents for remediation of noxious pollutants from wastewater. Environ. Int. 127, 160–180.
Avant, B., Bouchard, D., Chang, X., Hsieh, H.-S., Acrey, B., Han, Y., Spear, J., Zepp, R., Knightes, C.D., 2019. Environmental fate of multiwalled carbon nanotubes and graphene oxide across different aquatic ecosystems. NanoImpact 13, 1–12.
Beryani, A., Moghaddam, M.R.A., Tosco, T., Bianco, C., Hosseini, S.M., Kowsari, E., Sethi, R., 2020. Key factors affecting graphene oxide transport in saturated porous media. Sci. Total Environ. 698, 134224.
Calandra, P., de Caro, T., Caschera, D., Lombardo, D., Todaro, L., Liveri, V.T., 2015. Spectroscopic and structural characterization of pure and FeCl 3-containing tri-n-butyl phosphate. Colloid Polym. Sci. 293 (2), 597–603.
Chen, C., Shang, J., Zheng, X., Zhao, K., Yan, C., Sharma, P., Liu, K., 2018. Effect of physicochemical factors on transport and retention of graphene oxide in saturated media. Environ. Pollut. 236, 168–176.
Chen, L., Li, J., Chen, Z., Gu, Z., Yan, L., Zhao, F., Zhang, A., 2020. Toxicological evaluation of graphene-family nanomaterials. J. Nanosci. Nanotechnol. 20 (4), 1993–2006.
Chowdhury, I., Duch, M.C., Mansukhani, N.D., Hersam, M.C., Bouchard, D., 2013. Colloidal properties and stability of graphene oxide nanomaterials in the aquatic environment. Environ. Sci. Technol. 47 (12), 6288–6296.
Crittenden, J.C., Harza, B.M.W., 2005. Water Treatment: Principles and Design. Wiley.
Dong, S., Sun, Y., Gao, B., Shi, X., Xu, H., Wu, J., Wu, J., 2017. Retention and transport of graphene oxide in water-saturated limestone media. Chemosphere 180, 506–512.
Fadeel, B., Bussy, C., Merino, S., Vázquez, E., Flahaut, E., Mouchet, F., Evariste, L., Gauthier, L., Koivisto, A.J., Vogel, U., 2018. Safety assessment of graphene-based materials: focus on human health and the environment. ACS Nano 12 (11), 10582–10620.
French, R.A., Jacobson, A.R., Kim, B., Isley, S.L., Penn, R.L., Baveye, P.C., 2009. Influence of ionic strength, pH, and cation valence on aggregation kinetics of titanium dioxide nanoparticles. Environ. Sci. Technol. 43 (5), 1354–1359.
Guo, M.-T., Zhang, G.-S., 2017. Graphene oxide in the water environment could affect tetracycline-antibiotic resistance. Chemosphere 183, 197–203.
Hasan, M.S., Geza, M., Vasquez, R., Chilkoor, G., Gadhamshetty, V., 2020. Enhanced heavy metal removal from synthetic stormwater using nanoscale zerovalent iron–modified biochar. Water, Air, Soil Pollut. 231, 1–15.
Huang, X.-M., Liu, L.-Z., Zhou, S., Zhao, J.-J., 2020. Physical properties and device applications of graphene oxide. Frontiers of Physics 15 (3), 33301.
Kim, D.-G., Hwang, Y.-H., Shin, H.-S., Ko, S.-O., 2016. Kinetics of nitrate adsorption and reduction by nano-scale zero valent iron (NZVI): effect of ionic strength and initial pH. KSCE Journal of Civil Engineering 20 (1), 175–187.
Lanphere, J.D., Luth, C.J., Walker, S.L., 2013. Effects of solution chemistry on the transport of graphene oxide in saturated porous media. Environ. Sci. Technol. 47 (9), 4255–4261.
Liang, Y., Bradford, S.A., Šimůnek, J., Klumpp, E., 2019. Mechanisms of graphene oxide aggregation, retention, and release in quartz sand. Sci. Total Environ. 656, 70–79.
Liao, C., Li, Y., Tjong, S., 2018. Graphene nanomaterials: synthesis, biocompatibility, and cytotoxicity. Int. J. Mol. Sci. 19 (11), 3564.
Liu, L., Zhang, J., Zhao, J., Liu, F., 2012. Mechanical properties of graphene oxides. Nanoscale 4 (19), 5910–5916.
Lu, X., Lu, T., Zhang, H., Shang, Z., Chen, J., Wang, Y., Li, D., Zhou, Y., Qi, Z., 2019. Effects of solution chemistry on the attachment of graphene oxide onto clay minerals. Environmental Science: Processes & Impacts 21 (3), 506–513.
Ma, F.-Y., 2012. Corrosive effects of chlorides on metals. Pitting corrosion 294, 139–178.
Messina, F., Marchisio, D.L., Sethi, R., 2015. An extended and total flux normalized correlation equation for predicting single-collector efficiency. J. Colloid Interface Sci. 446, 185–193.
Norouzi, O., Di Maria, F., 2018. Catalytic effect of functional and Fe composite biochars on biofuel and biochemical derived from the pyrolysis of green marine biomass. Fermentation 4 (4), 96.
Omidvar, A., RashidianVaziri, M., Jaleh, B., Shabestari, N.P., Noroozi, M., 2016. Metal-enhanced fluorescence of graphene oxide by palladium nanoparticles in the blue–green part of the spectrum. Chin. Phys. B 25 (11), 118102.
Poulin, P., Jalili, R., Neri, W., Nallet, F., Divoux, T., Colin, A., Aboutalebi, S.H., Wallace, G., Zakri, C., 2016. Super flexibility of graphene oxide. Proc. Natl. Acad. Sci. Unit. States Am. 113 (40), 11088–11093.
Prabu, D., Parthiban, R., Ponnusamy, S.K., Anbalagan, S., John, R., Titus, T., 2017. Sorption of Cu (II) ions by nano-scale zero valent iron supported on rubber seed shell. IET Nanobiotechnol. 11 (6), 714–724.
Qi, Z., Du, T., Ma, P., Liu, F., Chen, W., 2019. Transport of graphene oxide in saturated quartz sand containing iron oxides. Sci. Total Environ. 657, 1450–1459.
Research, T.M., 2016. Graphene Market - Global Industry Analysis, Size, Share, Growth, Trends and Forecast 2015 - 2023.
Rodríguez-Vila, A., Selwyn-Smith, H., Enunwa, L., Smail, I., Covelo, E.F., Sizmur, T., 2018. Predicting Cu and Zn sorption capacity of biochar from feedstock C/N ratio and pyrolysis temperature. Environ. Sci. Pollut. Control Ser. 25 (8), 7730–7739.
Sleiman, N., Deluchat, V., Wazne, M., Mallet, M., Courtin-Nomade, A., Kazpard, V., Baudu, M., 2017. Phosphate removal from aqueous solutions using zero valent iron (ZVI): influence of solution composition and ZVI aging. Colloid. Surface. Physicochem. Eng. Aspect. 514, 1–10.
Smith, A.T., LaChance, A.M., Zeng, S., Liu, B., Sun, L., 2019. Synthesis, properties, and applications of graphene oxide/reduced graphene oxide and their nanocomposites. Nano Materials Science 1 (1), 31–47.
Sun, Y., Gao, B., Bradford, S.A., Wu, L., Chen, H., Shi, X., Wu, J., 2015. Transport, retention, and size perturbation of graphene oxide in saturated porous media: effects of input concentration and grain size. Water Res. 68, 24–33.
Teng, Z., Shao, W., Zhang, K., Yu, F., Huo, Y., Li, M., 2020. Enhanced passivation of

lead with immobilized phosphate solubilizing bacteria beads loaded with biochar/nanoscale zero valent iron composite. J. Hazard Mater. 384, 121505.
Thompson, K.A., Shimabuku, K.K., Kearns, J.P., Knappe, D.R., Summers, R.S., Cook, S.M., 2016. Environmental comparison of biochar and activated carbon for tertiary wastewater treatment. Environ. Sci. Technol. 50 (20), 11253–11262.
Wang, J., Zhu, M., Chen, Z., Chen, Y., Hayat, T., Alsaedi, A., Wang, X., 2019. Polyacrylamide modified molybdenum disulfide composites for efficient removal of graphene oxide from aqueous solutions. Chem. Eng. J. 361, 651–659.
Wang, K., Ruan, J., Song, H., Zhang, J., Wo, Y., Guo, S., Cui, D., 2011. Biocompatibility of graphene oxide. Nanoscale Res Lett 6 (1), 8.
Wang, M., Gao, B., Tang, D., Sun, H., Yin, X., Yu, C., 2017. Effects of temperature on graphene oxide deposition and transport in saturated porous media. J. Hazard Mater. 331, 28–35.
Wei, N., Peng, X., Xu, Z., 2014. Breakdown of fast water transport in graphene oxides. Phys. Rev. 89 (1), 012113.
Xiong, J., Ren, S., He, Y., Wang, X.C., Bai, X., Wang, J., Dzakpasu, M., 2019. Bioretention cell incorporating Fe-biochar and saturated zones for enhanced stormwater runoff treatment. Chemosphere 237, 124424.
Xu, J., Liu, X., Cao, Z., Bai, W., Shi, Q., Yang, Y., 2020. Fast degradation, large capacity, and high electron efficiency of chloramphenicol removal by different carbon-supported nanoscale zerovalent iron. J. Hazard Mater. 384, 121253.
Yuan, L., Tian, M., Lan, J., Cao, X., Wang, X., Chai, Z., Gibson, J.K., Shi, W., 2018. Defect engineering in metal–organic frameworks: a new strategy to develop applicable actinide sorbents. Chem. Commun. 54 (4), 370–373.
Zhang, C., Yan, A., Wang, G., Jin, C., Chen, Y., Shen, C., 2018a. Impact of flow velocity on transport of graphene oxide nanoparticles in saturated porous media. Vadose Zone J. 17 (1).
Zhang, S., Yang, X., Liu, L., Ju, M., Zheng, K., 2018b. Adsorption behavior of selective recognition functionalized biochar to Cd (II) in wastewater. Materials 11 (2), 299.
Zhu, Y., Murali, S., Cai, W., Li, X., Suk, J.W., Potts, J.R., Ruoff, R.S., 2010. Graphene and graphene oxide: synthesis, properties, and applications. Adv. Mater. 22 (35), 3906–3924.